Faculteit Bètawetenschappen

Finding Dirac Cones in Two Dimensional Artificial Lattices

Bachelor Thesis

Wies Uijttewaal

Natuur- en Sterrenkunde

Supervisors:

Prof. Dr. Cristiane de Morais Smith
Institute for Theoretical Physics

Guido van Miert MSc.
Institute for Theoretical Physics

February 2018

Abstract

The focus of this thesis lies on finding Dirac cones in band structures of two dimensional artificial lattices. These special band crossing points (BCP's) indicate interesting electronic properties of the material. In two dimensional systems, the symmetry of the lattice determines whether BCP's occur. Graphene, with its hexagonal lattice structure, is the best known 2D material that contains Dirac cones. Our goal is here to look for Dirac cones in two dimensional artificial square lattices. Using the symmetries of the square, we try to find Dirac cones in the band structure. To create these lattices artificially, we use the nearly free electron model as an approximation to the tight binding model describing a crystal. This approximation is valid for low energy ranges. Using three different types of lattices, each defined by a different potential landscape, we find Dirac cones emerging in two of them.

Contents

1 Introduction

The atomic structure of materials largely determines their electronic properties. The conductivity of metals arises from their crystalline structure through which loosely bound electrons travel. Insulators, on the other hand, do not conduct electricity and semi-conductors are somewhere in between. These differences stem from the range of energies, the electronic band structure, which electrons in a material may occupy. Figure 1 shows the band structures of metals, insulators and semiconductors. Metals have partially filled bands and empty states at the Fermi level, allowing charge transport through the material. Insulators have completely filled bands separated by a large gap, allowing no transport to take place. Between these two types of materials, semi-conductors have nearly filled bands and only a small band gap, making charge transport possible in certain conditions depending on, for example, temperature.
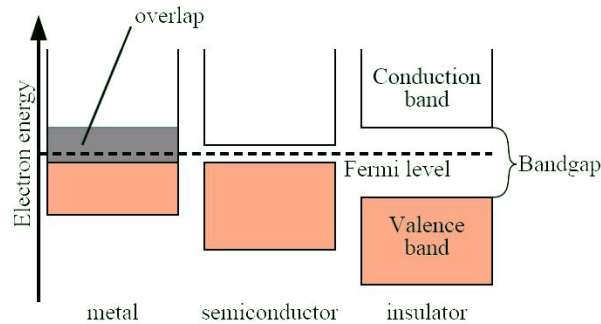

Figure 1: Metals have no band gap at the Fermi level. The valence band and the conduction band overlap allowing charge transport. Insulators show a large gap at the Fermi level, prohibiting charge transport. Semiconductors have a small band gap, which can be bridged in certain conditions. Figure is taken from `https://archive.cnx.org/contents/d1c4c0c9-7bcb-4245-b320-6d6fdb3ade9e@1/band-gap` on November 3, 2017.

In addition to ordinary materials, one may also consider artificial lattices. The interest in these artificial lattices is manifold. Firstly, it allows us to design any structure we want. Moreover, as opposed to the crystal lattice structure of existing metals, using these synthetically crafted structures gives us a much higher level of control. Therefore, we can precisely study the effect of defects or strain on the electronic properties.
The research into these synthetic structures focuses mainly on the study of electronic properties of materials. It offers a theoretical approach to the the structure of metals, semi-conductors and insulators which may lead to new insights into their electronic properties. Alternatively, it may also function as a doorway to the creation of new materials with certain desired properties, such as Dirac-type energy bands. Dirac cones emerge at the linear crossing point of two energy bands.

In this thesis, we address the question *"Can we find Dirac cones in two dimensional artificial lattices?"*. We shall focus especially on the contribution of symmetry to the emergence of this phenomenon.
There are various ways of creating artificial lattices in a lab. Periodic wave guides can be used to trap light creating a photonic crystal and lasers are used to position ultra-cold atoms in a certain configuration [1]. Another method that is often used to study band structures and other electronic properties with are quantum dot arrays. Quantum dots are nanoscale particles that behave like artificial atoms with discrete electronic states and are therefore ideally suited for studying the properties of artificial lattices. An artificial lattice may also be created on a flat copper or lead surface using carbon monoxide molecules [2]. These molecules are placed in a certain structural pattern on top of a copper or lead surface using a scanning tunneling microscope. This creates a potential landscape which determines where the electrons in the material are allowed to be. Lithography, the etching away of atoms from a surface, uses a similar procedure, but instead of creating areas where electrons are allowed, it creates holes where electrons are not allowed [3].

The electrons in a crystalline material can be modelled using an atomic tight binding model (TB). This method takes into account the atomic lattice structure of the system and the interaction between the elec-

trons and ions. Each atom is described by a set of orbitals in which electrons may occupy a certain energy. When orbitals of neighbouring atoms overlap, a dispersive energy band is formed. Theoretical research of this nature has been done for example on two dimensional honeycomb lattices [4].

Another model used to describe electron behaviour in a crystal is the nearly free electron model (NFE). The band structure derived from this model is determined by the dispersion relation of a free particle with an effective mass in a potential field. If a lattice structure is replaced by a nearly free electron model, then the information pertaining to that lattice is encoded in the effective mass. An advantage of the NFE model is its malleability. Complicated lattice structures are easily translated to a potential landscape, making calculations of the band structure less complex.

In the first part of this thesis, we shall take a closer look at these two models and assess whether and under which conditions the nearly free electron model can be used as an approximation to the tight binding model for one dimensional systems. In the second part, we use this model to create an artificial lattice in two dimensions, which we then manipulate in order to find Dirac cones.

2 One Dimensional Lattices
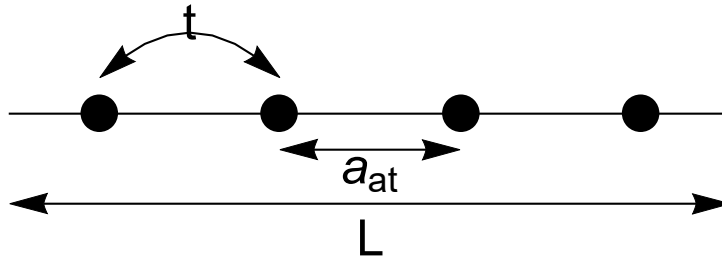
2.1 Tight Binding Model

Figure 2: A representation of a one dimensional lattice of length L, with a hopping parameter t, atomic lattice constant a_{at} and superlattice constant a_s.

The tight binding model describes electrons in a lattice. This model assumes that electrons are tightly bound to the atoms to which they belong. The interaction with potentials on neighbouring sites is limited. The basis for this model is a one dimensional infinite chain of atoms, or sites, separated by the atomic lattice constant a_{at}. In this case only nearest neighbour 'hoppings' are included through a hopping parameter t. This parameter allows the electrons to move from one site (or atom) to the next. The on-site energy is given by E_0. The Hamiltonian for a simple one dimensional tight binding model is given by:

$$H = t \sum_i |i\rangle\langle i+1| + h.c. + E_0 \sum_i |i\rangle\langle i| \tag{2.1}$$

where i denotes the lattice site and $h.c.$ is the hermitian conjugate expression. To find the eigenvalues and eigenvectors of the system, we will exploit the translation symmetry. Using a Fourier transformation, we find that the wave function is given by:

$$|k\rangle = \sum_j e^{ikja_{at}}|j\rangle, \tag{2.2}$$

where a_{at} denotes the atomic lattice constant and k the momentum. Acting with H on $|k\rangle$, we find:

$$H|k\rangle = [E_0 + 2t\cos(ka_{at})]|k\rangle. \tag{2.3}$$

Thus, the band structure for a simple one dimensional, infinite lattice is given by: $E(k) = E_0 + 2t\cos(ka_{at})$.

2.2 Nearly Free Electron Model

For small values of ka_{at}, this energy can be approximated by

$$E_{TB} \simeq E_0 + 2t(1 - \frac{(ka_{at})^2}{2}). \tag{2.4}$$

The first two terms in this equation can be seen together as an on-site energy, such as the Coulomb interaction of the electron with the ion at that site. The third term is quadratic in the momentum, which makes it similar to the dispersion relation of a free electron gas ($E_{FE} = \frac{\hbar^2 k^2}{2m}$, with mass $m = m_e$). This suggests that, if $|ka_{at} \ll 1|$, electrons in the lattice behave as free particles and that the nearly free electron model can be used as an approximation to an intricate tight binding lattice. In the nearly free electron model, the ionic lattice structure used in tight binding is replaced by a free electron gas with an effective mass. If a periodic potential is added to this lattice, the energies of the free electrons, which are described by a time independent Schrödinger equation (2.5), can be solved using Bloch's Theorem.

The periodic potential creates a superlattice with lattice constant a_s. For simplicity, a_s is considered here as

a multiple of the atomic lattice constant a_{at}, but this is not a general restriction. For the one dimensional case, we consider a chain of atoms of length L with periodic boundary conditions. The atomic lattice constant is denoted by a_{at}. This is also shown in Figure 4.

The Schrödinger equation for electrons in a one dimensional lattice is given by:

$$H = \frac{p^2}{2m^*} + V. \tag{2.5}$$

The Bloch Theorem states that the set of eigenfunctions of an electron in a system with a periodic potential has the same periodicity as that potential. The periodic potential creates a superlattice in which

$$V(x + a_s) = V(x),$$

with a_s the lattice constant of the superlattice. The Bloch Theorem then states that the set of eigenfunctions must also meet this condition, up to a phase factor ϕ:

$$\psi_{k,n}(x + a_s) = \psi_{k,n}(x)e^{ika_s},$$

where $\psi_{k,n}(x)$ is chosen as:

$$\psi_{k,n}(x) = e^{ikx}u_{k,n}(x), \tag{2.6}$$

with k the momentum, n the band index and $u_{k,n}$ periodic. The allowed momenta from the periodic boundary condition of the finite chain are then: $k_j = \frac{2\pi j}{L}$.

Using the Bloch waves, the Schrödinger equation becomes:

$$\left(\frac{p^2}{2m^*} + \frac{\hbar k}{m^*}p + \frac{\hbar^2 k^2}{2m^*} + V(x) \right) u_{k,n}(x) = E_n(k)u_{k,n}(x). \tag{2.7}$$

This can be simplified, resulting in the following expression:

$$\left(\nabla^2 + 2ik\partial_x - k^2 - \frac{2m^*}{\hbar^2}V \right) u_{k,n}(x) = -\frac{2m^*}{\hbar^2}E_n(k)u_{k,n}(x). \tag{2.8}$$

2.3 Comparing the NFE and TB Models

The NFE model is not always a good approximation for the TB model. Away from the band bottom, the influence of the lattice plays an important role in the TB model. Figure 3 shows the NFE and the TB model without the presence of an external potential. The region in which NFE model can apply as an approximation is $k \cdot a_s \in [-0.8, 0.8]$. The maxima of the band can also be approximated by a NFE model, using a negative effective mass. In that case the conductivity of the system is determined by holes moving through the lattice instead of electrons.
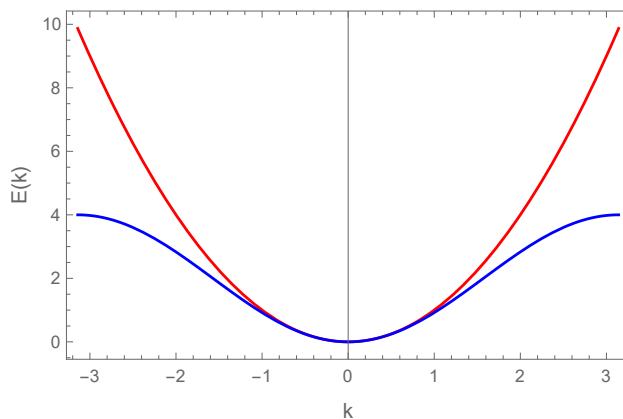

Figure 3: The dispersion relations of the NFE model (red) and of the TB model (blue) on the first Brillouin zone without an external potential

2.4 Dimensions

In order to compare the eigenenergies given by the TB model to the dispersion relations of the NFE model, their energies must be given in the same dimensions.

Firstly, the hopping parameter in the TB model can be fixed, which also fixes the fundamental physical constants in the Schrödinger equation (2.5) of the NFE model. Ignoring the on-site energy term, the tight binding energy $E_{TB} \simeq -t(ka_{at})^2$ can be equated with the energy of a free particle with effective mass m^*, $E_{NFE} = \frac{\hbar^2 k^2}{2m^*}$. This results in an expression for t:

$$t = -\frac{\hbar^2}{2m^*}, \tag{2.9}$$

where a_{at} is taken to be 1. Therefore, if we take $t = -1$, then $-\frac{\hbar^2}{2m^*} = -1$.

Secondly, it is important to consider the energies on the same domain when comparing both models. The first Brillouin zone is defined on the region of $k \in [-\frac{\pi}{a_s}, \frac{\pi}{a_s}]$ and thus $k \cdot a_s \in [-\pi, \pi]$.

These two choices result in a Schrödinger equation which gives a dimensionless energy:

$$\left(\nabla^2 + \frac{2ik}{a_s}\partial_x - \frac{k^2}{a_s^2} - V\right)u_{k,n}(x) = -E_n(k \cdot a_s)u_{k,n}(x). \tag{2.10}$$

2.5 Adding an External Potential

In order to study the electronic properties of materials, a superlattice is created on top of the atomic lattice via the external potential V. For simplicity, the periodicity of this potential is again taken to be a multiple of the atomic lattice constant, thereby creating unit cells as seen in Figure 4. The tight binding Hamiltonian of such a system is given by:

$$H = \sum_i t[|i,1\rangle\langle i,2| + |i,2\rangle\langle i,3| + \cdots + |i,n\rangle\langle i+1,1|] + h.c. + \sum_i \sum_\alpha^n V_\alpha|i,\alpha\rangle\langle i,\alpha| \tag{2.11}$$

where i indicates the unit cell in the superlattice, α the n-th atom in the unit cell, t the hopping parameter and V_α the external potential at lattice site α.
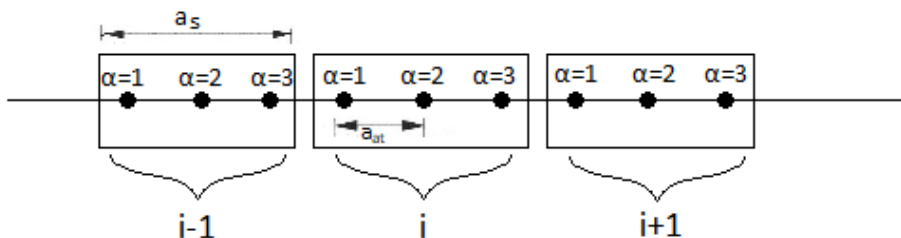

Figure 4: A one dimensional lattice with three atoms in each unit cell i of the superlattice.

An example of such a superlattice is shown in Figure 4, where the potential is periodic over three atomic lattice sites. For a superlattice with unit cells containing $n = 3$ atoms and an external potential $V_\alpha = v_0 \cos(\frac{2\pi}{a_s}\alpha \cdot a_{at} + \phi)$, the Hamiltonian is given by:

$$H = \begin{pmatrix} v_0\cos(\frac{2\pi}{3} + \phi) & t & te^{ika_s} \\ t & v_0\cos(2\frac{2\pi}{3} + \phi) & t \\ te^{-ika_s} & t & v_0\cos(3\frac{2\pi}{3} + \phi) \end{pmatrix}. \tag{2.12}$$

To determine the ideal size of the unit cells for the superlattice, a cosine potential will be used. Note that this potential has a phase which is trivial in the NFE model, but not in the TB model. As Figure 5

shows, the dispersion relation in the TB model is dependent on the phase ϕ of the potential. However, this dependency is less important for lower values of the potential, indicated by a smaller v_0 (compare Figures 5b and 5a). The phase dependency also decreases for larger unit cells, as is shown in Figure 5c. In the case of the NFE model, there is no phase dependency, which can be seen in Figure 5d.

For $n = 3$, Figure 6a shows the energy bands of both the NFE model as well as the TB model. For higher bands, the tight binding approximation is clearly not optimal in this case. Figure 6c shows that this approximation is valid when $n = 30$. Hence, in the low energy range (or for large unit cells) the NFE model is a good approximation to the TB model. We use this result in Chapter 4 to create artificial lattices in two dimensions.

(a) $v_0 = 1.4$, $n = 3$ (b) $v_0 = 0.4$, $n = 3$

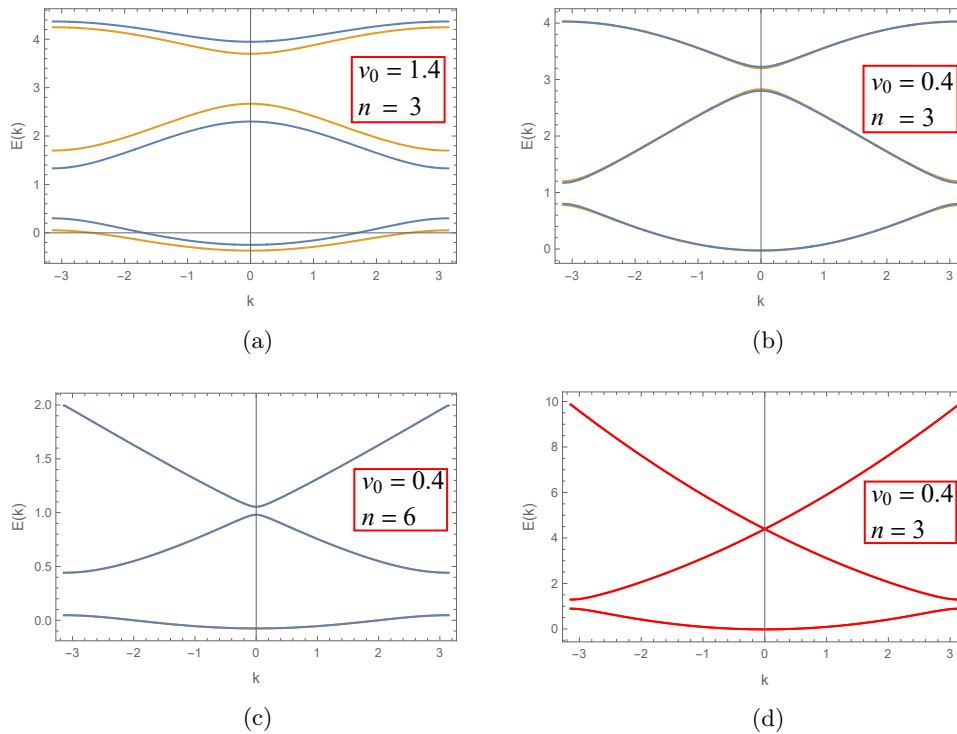(c) $v_0 = 0.4$, $n = 6$ (d) $v_0 = 0.4$, $n = 3$

Figure 5: 5a, 5b and 5c show the phase dependency of the TB energy dispersion ($\phi = 0$ yellow, $\phi = \pi$ blue). When the strength of the external potential (v_0) is decreased, this dependency becomes less important. It becomes even less important when the size of the unit cell (n) is increased. 5d shows that the NFE model (red) is not dependent on the phase of the potential.
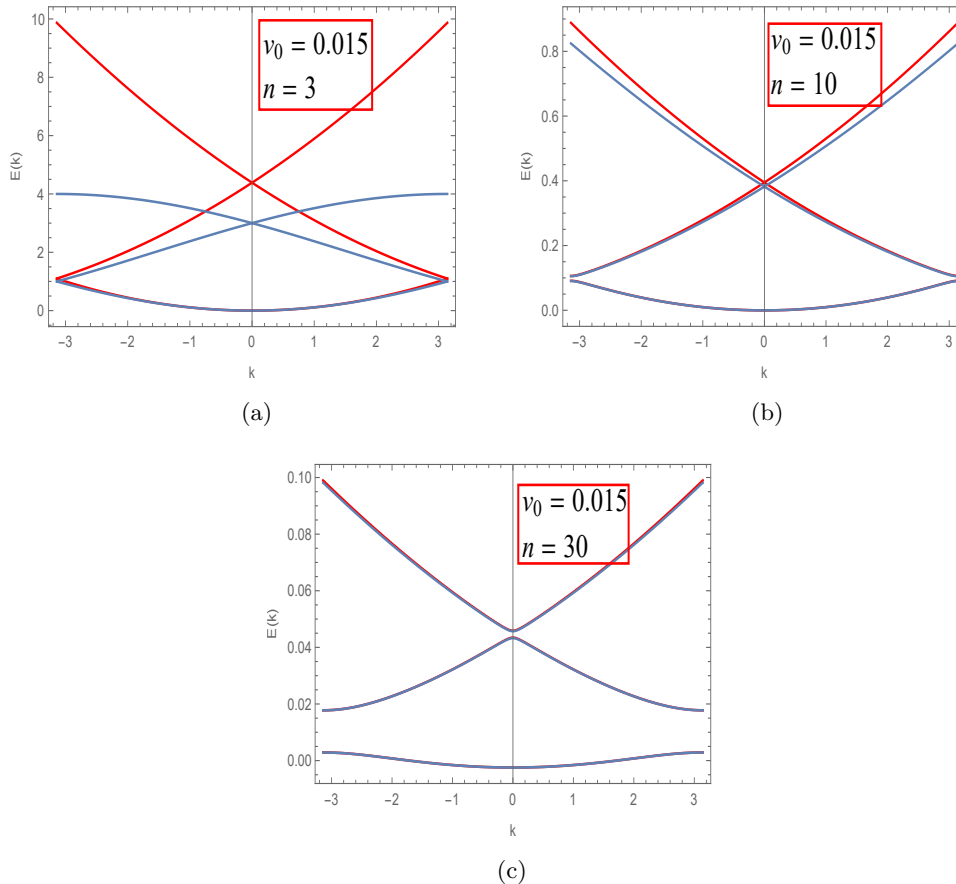
(a)

(b)

(c)

Figure 6: The dispersion relation for the NFE model (red) and the eigenvalues of the TB model (blue) when an external cosine potential is applied to the lattice. In Figure 6a, the unit cell of the superlattice contains 3 atoms, $v_0 = 0.015$ and $\phi = \pi$. Although the lowest energy bands are comparable, the other two are clearly not. As we increase the number of atoms in the unit cell, the energy bands given by the NFE model and the TB model approach each other. In 6c the unit cell contains 30 atoms, $v_0 = 0.015$ and $\phi = \pi$. In this case, the NFE model is a good approximation to the TB model for all three bands.

2.6   Effective Mass Theorem

A method often applied to treat perturbations of a tight binding system, such as lattice defects, impurity atoms or applied electric or magnetic fields, is the Effective Mass Theorem (EMT). In Appendix A, a derivation of this theorem is given.

In our case, the theorem may be used to relate the results obtained from the TB model and the NFE model. The effective mass theorem simplifies the behaviour of electrons which move in a periodic potential much greater than the atomic lattice constant ($a_s \gg a_{at}$). It replaces the full Hamiltonian by an effective Hamiltonian based on the energy dispersion of the unperturbed crystal. In particular, it shows that the wave function obtained through the NFE model corresponds to the envelope wave function, F. As a result, the NFE model does not describe the shape of the wave function at the atomic scale.

3   Two Dimensional Lattices

The focus of this thesis lies on two dimensional band structures. In one dimensional systems, band structures consist only of single bands which do not cross, e.g. they are non-degenerate systems. Two dimensional systems, however, are a completely different picture altogether. The best known and researched example of a two dimensional material is graphene [5]. This material exhibits degenerate eigenvalues: points where two energy bands cross and the energy gap between them is 0. These band crossing points (BCP's) can indicate interesting electronic properties of the material. A band crossing point from which the two bands disperse linearly is called a Dirac cone. Examples of lattices which show Dirac cones in the band structure are the honeycomb lattice seen in graphene and the Kagome lattice. The checkerboard lattice has band crossing points from which the bands disperse quadratically. It turns out that the presence of BCP's can be traced back to a symmetry in the two dimensional lattice. This is treated in section 3.1. Afterwards, we shall go into more detail about the structure of graphene in section 3.2.

Aside from the hexagonal lattice, other symmetrical structures may be considered for the study of BCP's, such as square lattices. It has been shown that the emergence of Dirac cones can be attributed to the mirror symmetries of the lattices [6]. Our goal is here to look for BCP's in two dimensional artificial lattices with square symmetry. In contrast to the procedure outlined in Chapter 1 of this thesis, where we observed artificial lattices using the tight binding model and the nearly free electron model in one dimensional systems, we now limit us to the nearly free electron model in two dimensions. Effectively, we consider a two dimensional electron gas which is restricted by a potential landscape, consisting of square unit cells from which discs have been cut where the electrons are not allowed. Using three different types of potential landscapes, we hope to find band structures containing band crossing points, and specifically Dirac cones.

3.1   Wigner von Neumann Theorem

Not all two dimensional systems exhibit band crossing points. The Wigner von Neumann theorem determines in which cases they may occur. For a generic two band model the Hamiltonian is given by

$$H(\vec{k}) = \vec{d}(\vec{k}) \cdot \vec{\sigma} + d_0(\vec{k}) \cdot \sigma_0, \tag{3.1}$$

where $\vec{\sigma}$ denotes the Pauli matrices, σ_0 the identity matrix, $\vec{d}$ a three dimensional vector and d_0 the on-site energy. The dispersion relation $E(\vec{k})$ can be calculated by diagonalising the Hamiltonian matrix, resulting in:

$$E^{\pm}(\vec{k}) = d_0(\vec{k}) \pm \sqrt{d_x^2 + d_y^2 + d_z^2}. \tag{3.2}$$

To obtain a degeneracy, we need $E^+(\vec{K}_{BCP}) = E^-(\vec{K}_{BCP})$ and thus $d_x(\vec{K}_{BCP}) = d_y(\vec{K}_{BCP}) = d_z(\vec{K}_{BCP}) = 0$. Put differently, to find such a $\vec{K}_{BCP}$, we need to consider the intersection of the three level sets $d_x^{-1}(0) \cap d_y^{-1}(0) \cap d_z^{-1}(0)$. In a one dimensional system, there is only one parameter (k_x) which determines the system. Therefore, the inverse function will correspond to points, which have no cross section. Therefore in one dimension, it is not possible to obtain a degeneracy.

In two dimensions, the system is determined by k_x and k_y. The level sets correspond to three lines, which can only intersect in a single point in a fine-tuned example. However, if due to some symmetry of the system one of the conditions is satisfied for all $\vec{k}$, e.g. $d_z(\vec{k}) = 0$, then $d_z^{-1}(0) = BZ$, and we find that the set of band crossing points is simply the intersection of the two lines corresponding to $d_x^{-1}(0)$ and $d_y^{-1}(0)$.

In three dimensions, the level set d_α^{-1} is a two dimensional surface. Two intersecting surfaces result in a line, and a line intersecting with a third surface result in two or more intersection points or the empty set. Therefore, we find that any three dimensional system can potentially exhibit degeneracies. Below, we will show explicitly that in graphene inversion and time reversal symmetry ensure that $d_z(\vec{k}) = 0$.

3.2   Graphene: Symmetries and Dirac Cones

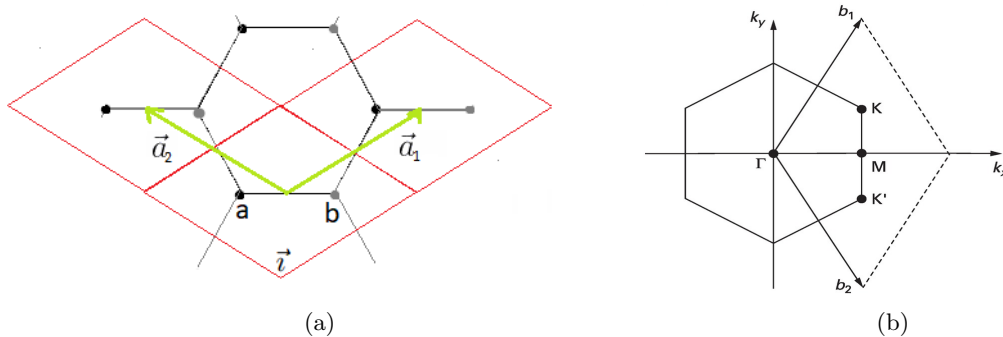(a)   (b)

Figure 7: Shown here is a schematic representation of graphene. Figure 7a shows the unit cell in direct space. The two atoms in the unit cell $\vec{\imath}$ are indicated by a, b. The lattice vectors are given by $\vec{a}_{1,2}$. Figure 7b shows the Brillouin Zone. Indicated are the Dirac cones at K and K', the reciprocal lattice vectors $\vec{b}_{1,2}$.

One material that exhibits Dirac cones is graphene. In this section, the band structure of a simple graphene model will be given and the different symmetries contributing to the existence and stability of the Dirac cones in graphene will be explained.

Figure 7a shows a schematic representation of graphene. The tight binding Hamiltonian corresponding to this lattice is given by:

$$H = -t \sum_{\vec{\imath}} [|a, \vec{\imath}\rangle\langle b, \vec{\imath}| + |a, \vec{\imath}\rangle\langle b, (i_1, i_2 - 1)| + |a, \vec{\imath}\rangle\langle b, (i_1 - 1, i_2)|] + h.c. \tag{3.3}$$

where a, b denote the two atoms in the unit cell $\vec{\imath} = (i_1, i_2)$. Here we have assumed that the hopping parameter t is the same between each pair of atoms ($t_1 = t_2 = t_3 = t$).

We define the wave functions for each of the atoms by:

$$|a/b, k\rangle := \sum_{\vec{\imath}} e^{i\vec{k}\cdot(i_1\vec{a_1} + i_2\vec{a_2})} |a/b, \vec{\imath}\rangle \tag{3.4}$$

in which $\vec{a}_{1,2}$ are the lattice vectors for the honeycomb graphene lattice. Including only nearest neighbour interactions and ignoring the on-site energy of the atoms, the Hamiltonian can be written as:

$$H = \int d\vec{k}(|a, \vec{k}\rangle, |b, \vec{k}\rangle) H(k) \begin{pmatrix} \langle a, \vec{k}| \\ \langle b, \vec{k}| \end{pmatrix}, \tag{3.5}$$

where

$$H(k) = -t \begin{pmatrix} 0 & 1 + e^{-i\vec{k}\cdot\vec{a_1}} + e^{i\vec{k}\cdot\vec{a_2}} \\ 1 + e^{i\vec{k}\cdot\vec{a_1}} + e^{-i\vec{k}\cdot\vec{a_2}} & 0 \end{pmatrix} \tag{3.6}$$

Figure 8 shows the eigenvalues of the tight binding Hamiltonian for graphene, in which the Dirac cones located at the K and K' points are clearly visible. In Figure 9, the energy bands are shown along the path $\Gamma \rightarrow M \rightarrow K \rightarrow \Gamma$ in the Brillouin Zone, also indicated in Figure 7b. This path, taken along the high symmetry points and lines of the lattice, functions as a cross section of the Brillouin Zone.
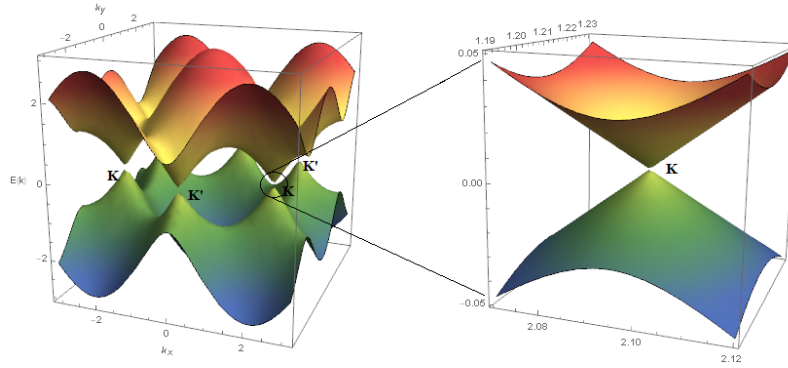
Figure 8: The eigenvalues of graphene and the Dirac cones located at points K and K'.
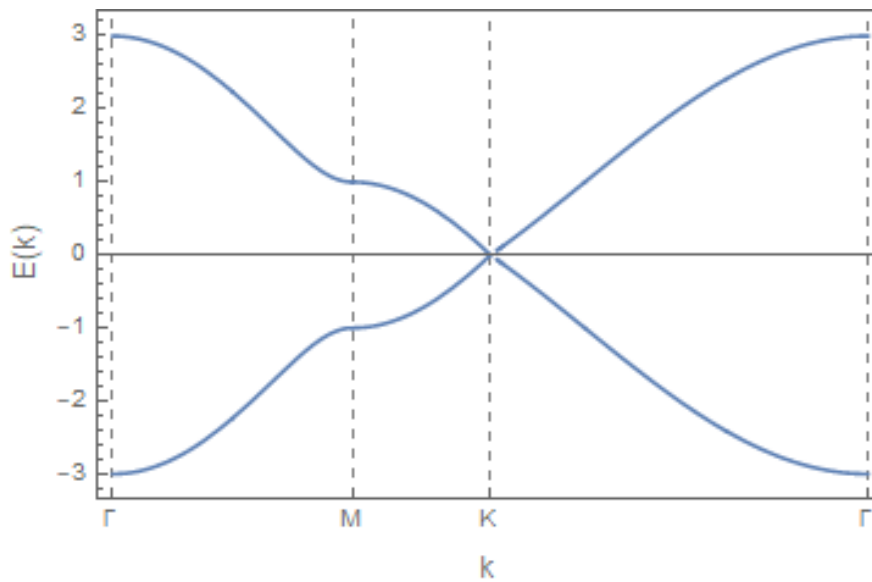

Figure 9: The band structure of graphene along the path $\Gamma \to M \to K \to \Gamma$.

In the previous section we have seen that in order for Dirac cones to occur, three conditions must be satisfied: $d_x = d_y = d_z = 0$. In the case of graphene, inversion and time reversal symmetry ensure that $d_z = 0$ is always satisfied. The other two conditions, $d_x = d_y = 0$, are satisfied only when $\vec{k} = \vec{K}$ or $\vec{K'}$. These high symmetry points occur due to the three-fold rotational symmetry of the lattice. In the following paragraphs, the contribution of each of these symmetries shall be made explicit.

3.3 Inversion Symmetry

For the derivation of the inversion and time reversal symmetry, we make use of chapters 4 and 7 in Bernevig's *Topological Insulators and Topological Superconductors* [7]. Inversion symmetry mirrors a lattice in both the x and y direction. For the graphene lattice shown in Figure 7a this means:

$$I|a, \vec{\imath}\rangle = |b, -\vec{\imath}\rangle$$

When we let the inversion operator work on the reciprocal wave vector, we get:

$$
\begin{aligned}
I|a, \vec{k}\rangle &= \sum_{\vec{i}} e^{i\vec{k}\cdot(i_1\vec{a_1}+i_2\vec{a_2})}|b, -\vec{i}\rangle \\
&= \sum_{\vec{j}} e^{i\vec{k}\cdot(-j_1\vec{a_1}-j_2\vec{a_2})}|b, \vec{j}\rangle \\
&= \sum_{\vec{j}} e^{i(-\vec{k})\cdot(j_1\vec{a_1}+j_2\vec{a_2})}|b, \vec{j}\rangle = |b, -\vec{k}\rangle.
\end{aligned}
\tag{3.7}
$$

The system is invariant under inversion if $[H, I] = 0$, or also $H = IHI^{-1}$. This results in:

$$
\begin{aligned}
\int d\vec{k}(|a, \vec{k}\rangle, |b, \vec{k}\rangle)H(k)\begin{pmatrix}\langle a, \vec{k}| \\ \langle b, \vec{k}|\end{pmatrix} &= \int d\vec{k}I(|a, \vec{k}\rangle, |b, \vec{k}\rangle)H(k)\begin{pmatrix}\langle a, \vec{k}| \\ \langle b, \vec{k}|\end{pmatrix}I \\
&= \int d\vec{k}(|b, -\vec{k}\rangle, |a, -\vec{k}\rangle)H(k)\begin{pmatrix}\langle b, -\vec{k}| \\ \langle a, -\vec{k}|\end{pmatrix} \\
&= \int d\vec{k}(|a, \vec{k}\rangle, |b, \vec{k}\rangle)\sigma_x H(-k)\sigma_x \begin{pmatrix}\langle a, \vec{k}| \\ \langle b, \vec{k}|\end{pmatrix}.
\end{aligned}
$$

Thus, inversion symmetry requires that

$$
H(\vec{k}) = \sigma_x H(-\vec{k})\sigma_x
\tag{3.8}
$$

3.4 Time Reversal Symmetry

Time reversal symmetry requires that a system regresses along the same path when time is reversed as it evolves. To understand how time reversal affects the Hamiltonian, we check how it affects the position and momentum operators:

$$
\begin{aligned}
T[\hat{x}, \hat{p}]T^{-1} &= T(i\hbar)T^{-1} \\
[\hat{x}, T\hat{p}T^{-1}] &= T(i\hbar)T^{-1} \\
-[\hat{x}, \hat{p}] = -i\hbar &= T(i\hbar)T^{-1}
\end{aligned}
$$

Only the momentum operator changes sign, because it is dependent on the velocity, which is a time derivative of the position invariant operator. This shows that the time reversal operator is proportional to the conjugation operator. This means that T is anti-unitarian. When the time reversal operator works on a Hamiltonian, it simply returns the complex conjugate of said Hamiltonian.
Once again, we can calculate what TR does to the Hamiltonian. If $[H, T] = 0$, then

$$
\begin{aligned}
\int d\vec{k}(|a, \vec{k}\rangle, |b, \vec{k}\rangle)H(k)\begin{pmatrix}\langle a, \vec{k}| \\ \langle b, \vec{k}|\end{pmatrix} &= \int d\vec{k}T(|a, \vec{k}\rangle, |b, \vec{k}\rangle)H(k)\begin{pmatrix}\langle a, \vec{k}| \\ \langle b, \vec{k}|\end{pmatrix}T^{-1} \\
&= \int d\vec{k}(|a, -\vec{k}\rangle, |b, -\vec{k}\rangle)TH(k)T^{-1}\begin{pmatrix}\langle a, -\vec{k}| \\ \langle b, -\vec{k}|\end{pmatrix} \\
&= \int d\vec{k}(|a, \vec{k}\rangle, |b, \vec{k}\rangle)TH(-k)T^{-1}\begin{pmatrix}\langle a, \vec{k}| \\ \langle b, \vec{k}|\end{pmatrix}.
\end{aligned}
$$

Time reversal symmetry requires that

$$
H(\vec{k}) = TH(-\vec{k})T^{-1} = H^*(-\vec{k})
\tag{3.9}
$$

Combining inversion and time reversal symmetry, we get $H(\vec{k}) = \sigma_x H^*(k)\sigma_x$, which if we take the generic Hamiltonian from equation (3.1) results in:

$$\vec{d}(\vec{k}) \cdot \vec{\sigma} + d_0(\vec{k}) \cdot \sigma_0 = \sigma_x(\vec{d}(\vec{k}) \cdot \vec{\sigma} + d_0(\vec{k}) \cdot \sigma_0)^* \sigma_x \tag{3.10}$$

$$d_x(\vec{k})\sigma_x + d_y(\vec{k})\sigma_y + d_z(\vec{k})\sigma_z + d_0(\vec{k})\sigma_0 = d_x(\vec{k})\sigma_x + d_y(\vec{k})\sigma_y - d_z(\vec{k})\sigma_z + d_0(\vec{k})\sigma_0. \tag{3.11}$$

Here we see that $d_z(\vec{k})$ must be equal to 0, which is one of the conditions for a band crossing point.

3.5 C_3 Symmetry

As we have just seen, one of the conditions for the Wigner von Neumann theorem has been satisfied by inversion and time reversal symmetry. This means that in the case of a two dimensional system the existence of Dirac points is possible. However, the presence of inversion and time reversal symmetry does not fix the position of the Dirac cones. This is done by the C_3 rotational symmetry of the lattice points.
Each point in the lattice can be rotated over $\frac{2\pi}{3}$, which corresponds to a cyclic permutation of the bond vectors connecting atom a with its neighbouring atoms b. The Dirac cones are stable when the off-diagonal elements of the Hamiltonian (3.6) are equal to 0. The equation $1 + e^{-i\vec{k}\cdot\vec{a_1}} + e^{i\vec{k}\cdot\vec{a_2}} = 0$ has two solutions: $K \cdot \vec{a_2} = \frac{2\pi}{3}$, $K \cdot \vec{a_1} = \frac{4\pi}{3}$ and $K' \cdot \vec{a_1} = \frac{2\pi}{3}$, $K' \cdot \vec{a_2} = \frac{4\pi}{3}$.

4 Artificial Square Lattices

In this thesis we look at three types of square lattices. Each type contains a different potential landscape, which determines the behaviour of the electrons. Type 1 is a square lattice from which a disc with diameter d_1 has been cut. At this disc, a potential approaching infinity has been placed, which serves as a restricted area for electrons. Periodic boundary conditions are placed on the boundaries of the square. An adaption of this primary lattice is type 2a, to which an extra disc on the corners of the unit cell has been added, with diameters $d_1 \leq d_2$. Lattices of type 2b contain three areas where an infinite potential excludes electrons, this time the added discs are located on the edges of the unit cell, with diameters $d_1 \leq d_2$. A schematic of these types is given in Figure 10.

The band structure is constructed using a Schrödinger equation for the NFE model similar to equation (2.10), but adapted to a two dimensional system:

$$\left(\vec{\nabla}^2 + 2i(\frac{k_x}{a_s}\partial_x + \frac{k_y}{a_s}\partial_y) - \frac{(k_x^2 + k_y^2)}{a_s^2} - V_\alpha \right) u_{k,n}(x,y) = -E_n(\vec{k} \cdot \vec{a_s})u_{\vec{k},n}(x,y), \tag{4.1}$$

where V_α indicates which type of lattice is used:

- $V_1 \to \infty$ for $x^2 + y^2 \leq \left(\frac{d_1}{2}\right)^2$

- $V_{2a} \to \infty$ for $x^2 + y^2 \leq \left(\frac{d_1}{2}\right)^2$, $(x - \frac{a_s}{2})^2 + (y - \frac{a_s}{2})^2 \leq \left(\frac{d_2}{2}\right)^2$, $(x + \frac{a_s}{2})^2 + (y - \frac{a_s}{2})^2 \leq \left(\frac{d_2}{2}\right)^2$, $(x - \frac{a_s}{2})^2 + (y + \frac{a_s}{2})^2 \leq \left(\frac{d_2}{2}\right)^2$, $(x + \frac{a_s}{2})^2 + (y + \frac{a_s}{2})^2 \leq \left(\frac{d_2}{2}\right)^2$

- $V_{2b} \to \infty$ for $x^2 + y^2 \leq \left(\frac{d_1}{2}\right)^2$, $(x - \frac{a_s}{2})^2 + y^2 \leq \left(\frac{d_2}{2}\right)^2$, $(x + \frac{a_s}{2})^2 + y^2 \leq \left(\frac{d_2}{2}\right)^2$, $x^2 + (y + \frac{a_s}{2})^2 \leq \left(\frac{d_2}{2}\right)^2$, $x^2 + (y - \frac{a_s}{2})^2 \leq \left(\frac{d_2}{2}\right)^2$
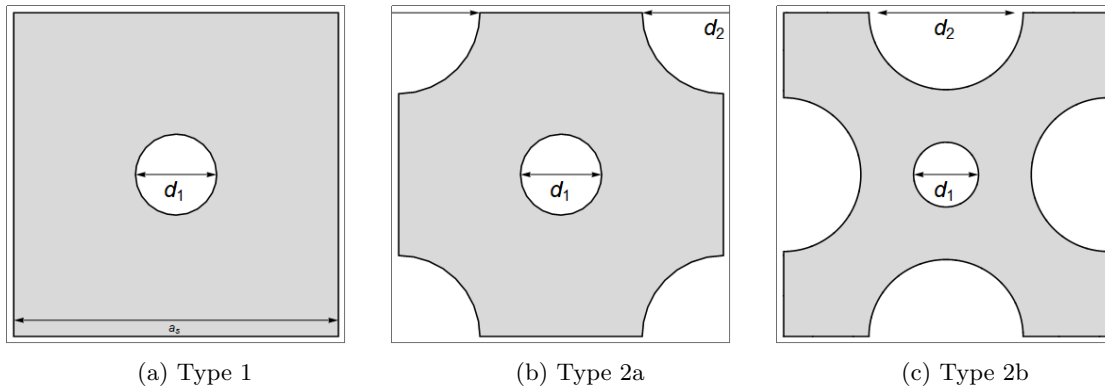

(a) Type 1　　　　　(b) Type 2a　　　　　(c) Type 2b

Figure 10: The three types of artificial lattices used to determine the presence of Dirac cones.
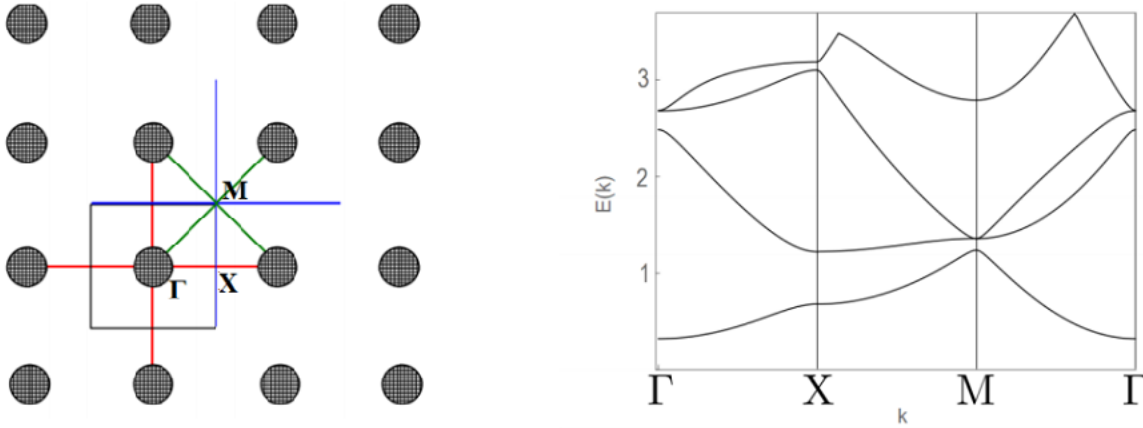
4.1 Lattice Type 1

Figure 11: The lattice structure and band energies for lattice type 1, with a disc/lattice ratio of $\frac{0.7}{4}$.
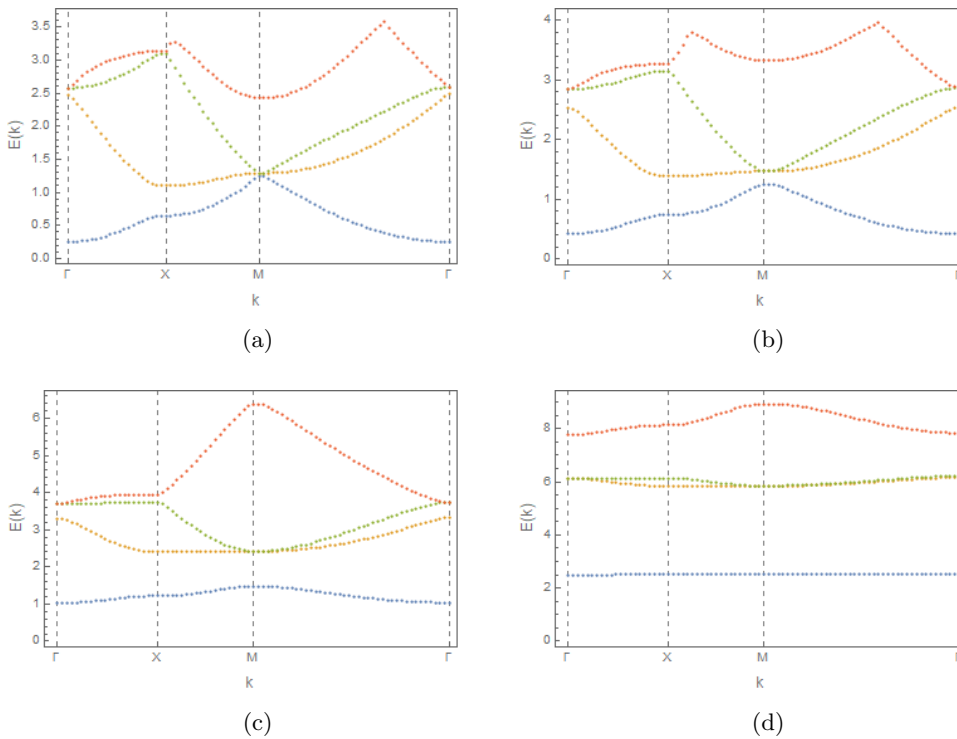

(a)

(b)

(c)

(d)

Figure 12: This figure shows the band structures for lattices of type 1, each with a different disc/lattice ratio. Graphs 12a, 12b, 12c and 12d have a ratio of $\frac{1}{8}, \frac{1}{4}, \frac{1}{2}$ and $\frac{3}{4}$ respectively. For each lattice, only the four lowest energy bands are shown along the path $\Gamma \to X \to M \to \Gamma$ in the Brillouin Zone.

Figure 11 shows the lattice and its mirror symmetries in more detail. There are three mirror symmetries in this simple lattice model. The band structure is plotted along the path $\Gamma \to X \to M \to \Gamma$ in the Brillouin Zone. The band structure in Figure 11 is a specific example for the disc/lattice ratio of $\frac{0.7}{4}$. Figure 12 shows the band structures for a number of lattices of type 1, each with a different disc/lattice ratio. From these band structures, we can form conclusions regarding the electronic properties of the lattice.

What we see in Figure 12a are the four lowest energy bands calculated along the same path. This band structure approaches the band structure of a free electron gas, which we saw in Figure 6a. The lowest band even approaches the form of a parabola, at least in the region $M \to \Gamma \to X$. This behaviour can be explained by the low disc/lattice ratio, which in this case is $\frac{d_1}{a_s} = \frac{1}{8}$. There is only a small region in the lattice where the electrons are not allowed. A free electron gas experiences no restrictions at all.

At M we can see the second and third band touch each other, while there is still a small gap between them and lowest band. This gap opens up when the diameter of the disc is increased. The greater the diameter, the more restricted the electrons are in their freedom and the material changes from a conductor to an insulator, which is the case in 12d. Between bands two and three, this band gap does not occur: there is a band crossing point. Whether level repulsion or band crossing points occur is determined by the eigenvalues of the symmetry operators $\hat{M}$ and $\hat{C}_4$. These operators are explained in more detail in Appendix B. Table 1 shows the eigenvalues for the symmetry operators of the energy bands for this band structure. At point M, the BCP is protected by the four-fold rotational symmetry of the lattice. We know that

$$\hat{C}_4 |a\rangle = i|a\rangle, \tag{4.2}$$

with $|a\rangle$ the wave function corresponding to an energy band at point M and $\hat{C}_4$ the rotation operator. For a system that is time reversal invariant, we can also write:

$$\hat{C}_4 T |a\rangle = T\hat{C}_4 |a\rangle == Ti|a\rangle = -iT|a\rangle. \tag{4.3}$$

Therefore, $\langle a|T|a\rangle = 0$. The eigenvalues are degenerate and we have a BCP at point M.

n	$\Gamma \to X$	$X \to M$	$M \to \Gamma$	M
1	+1	-1	+1	-1
2	+1	+1	-1	+i
3	-1	-1	+1	-i
4	+1	+1	+1	+1

Table 1: The symmetries of the various energy bands (labelled n) in the Brillouin Zone for Figure 12b. The first three columns show the eigenvalues of the mirror operator $\hat{M}$. The fourth column shows the eigenvalues for the four-fold rotation operator $\hat{C}_4$.

However, the BCP at M is not an actual Dirac cone, as the bands do not disperse linearly from the degeneracy. Hence, we must look at a different model. Here, we will double the original unit cell, while keeping the square symmetry. This can be done in two distinct ways.
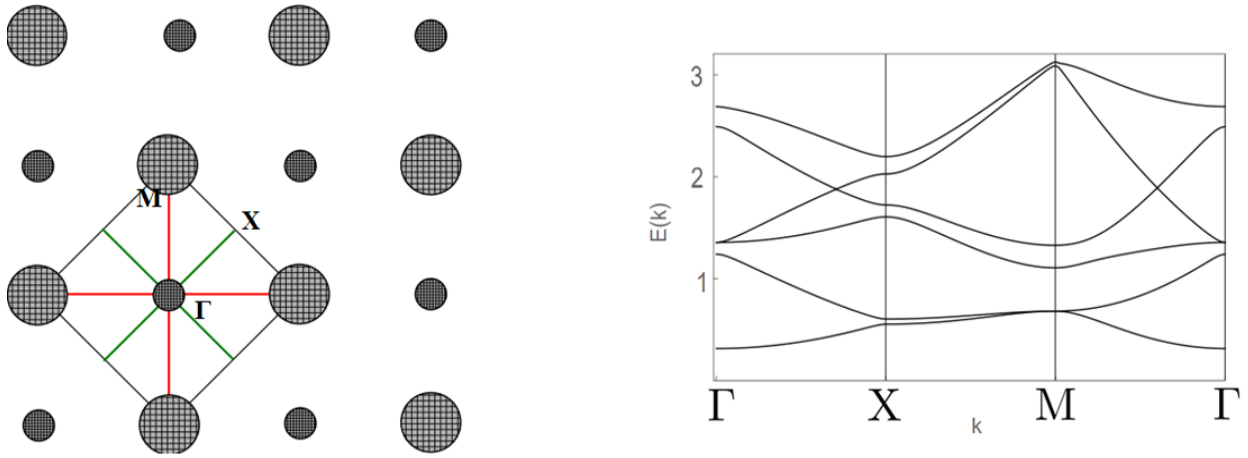
4.2 Lattice Type 2a

Figure 13: A type 2a lattice and its corresponding band energies taken along the path $\Gamma \to X \to M \to \Gamma$. The disc/lattice ratios are $\frac{d_1}{a_s} = \frac{0.6}{4\sqrt{2}}$ and $\frac{d_2}{a_s} = \frac{0.8}{4\sqrt{2}}$.

Type 2a is an example of a more complicated lattice structure. The unit cell is doubled in size and the potential discs on the corners are increased in size with respect to the central disc. Instead of the original symmetries (indicated with blue, green and red in Figure 11), only two symmetries are preserved. The blue symmetry is broken due to the alternating sizes of the discs. This results in a more complicated band structure, an example of which is shown in Figure 14. Since we doubled the size of the unit cell, there are now six energy bands instead of four in the same energy range as in the case of lattice type 1.

Again, there are several points of interest that can be located in the band structure. There are band crossing points at M (bands 1 and 2) and Γ (bands 3 and 4).

Clearly visible are two BCP's in the fourth and fifth band along the high symmetry lines $\Gamma \to X$ (green symmetry) and $M \to \Gamma$ (red symmetry). The bands do display linear dispersion around these points, which mean that we are dealing with Dirac cones. No level repulsion takes place as the bands have opposite mirror symmetry eigenvalues.
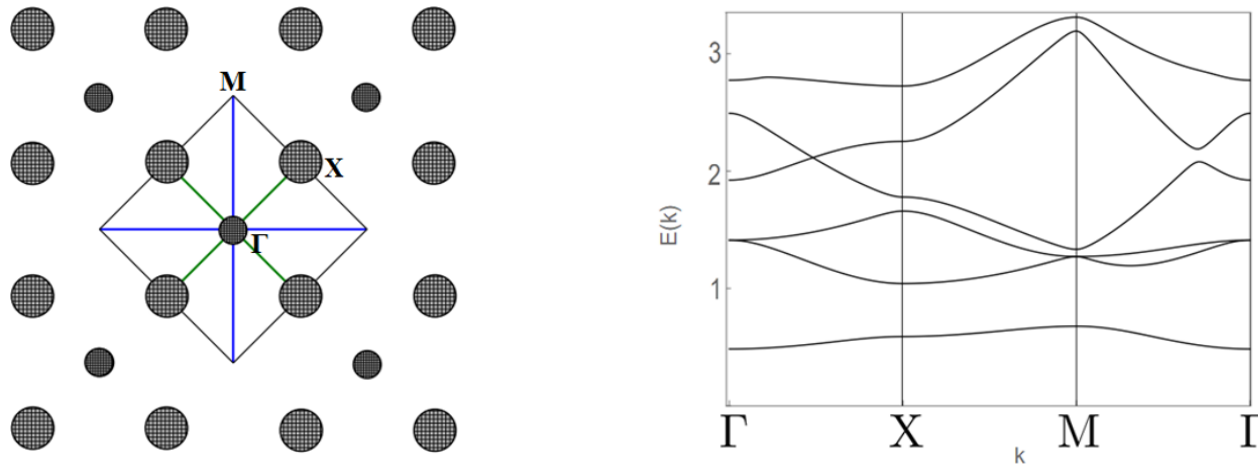
4.3 Lattice Type 2b

Figure 14: A type 2b lattice and its corresponding band energies taken along the path $\Gamma \to X \to M \to \Gamma$. The disc/lattice ratios are $\frac{d_1}{a_s} = \frac{0.5}{4\sqrt{2}}$ and $\frac{d_2}{a_s} = \frac{0.7}{4\sqrt{2}}$.

We can alter the simple lattice in a different way as well. Type 2b consists of a unit cell that has been doubled in size with an extra potential disc placed in the center of each unit cell. This configuration conserves the blue and green symmetries.

The band structure of type 2b is similar to that of type 2a, although the position of some of the BCP's has shifted. The lowest energy band is isolated once again, and the BCP's are now located at Γ (bands 2 and 3) and M (bands 2 and 3). However, the BCP between bands 4 and 5 is much more interesting. Similar to the previous case, there is a Dirac cone along the line $\Gamma \to X$ (green symmetry). However, whereas type 2a also showed a Dirac cone along $M \to \Gamma$, type 2b shows level repulsion. We can explain this by looking at the symmetries of the lattice. Lattices of type 2b only exhibits the blue and green symmetry, and thus the Dirac cone along the green line is conserved, while the Dirac cone along the red line has disappeared. Energy bands 4 and 5 correspond to eigenfunctions with the same symmetry along the path $M \to \Gamma$.

5 Conclusion, Discussion and Outlook

5.1 Conclusion

The purpose of this thesis is to create an artificial lattice that contains Dirac cones, using a nearly free electron model (NFE). We specifically focus on the symmetries of the (square) lattice which contribute to this phenomenon. In Chapter 2 we have seen that the NFE model, which describes the behaviour of a particle in a potential landscape, can be valid approximation for the tight binding model (TB model) for the one dimensional system. However, this validity depends on the size of the unit cell of the superlattice (e.g. the potential landscape). A large unit cell ensures that we stay in the low energy regions where the TB model can be approximated by a quadratic dispersion. The Effective Mass Theorem shows us that in this low energy range, the effects of the atomic lattice are of little importance. It is therefore a localised solution.

Having established that the nearly free electron model is a valid approximation with which to describe lattices, we can use it to create a two dimensional artificial lattice. In Chapter 3 we analyse the conditions necessary for the emergence of Dirac cones in two dimensional materials, taking graphene as an illustrative example. From Wigner von Neumann's theorem we infer that for two dimensional systems, the symmetry of the lattice is vital for the existence of band crossing points in general, and Dirac cones in particular. Therefore, in Chapter 4 we create three types of square lattices, each of which contains a certain set of mirror symmetries. Lattice type 1 contains three sets of symmetries. Although the band structure derived from it shows a band crossing point on the high symmetry point M of the Brillouin Zone, it does not contain Dirac cones. These linear crossings do emerge, however, in two adaptations of the basic lattice type 1. The band structure of type 2a shows two Dirac cones, located on the high symmetry lines in the Brillouin Zone. The symmetries contributing to this are the red and the green symmetry of the original lattice. Type 2b only shows one Dirac cone, located on the diagonal high symmetry line. Because the red symmetry is broken in this lattice, the second Dirac cone has disappeared. On the blue symmetry, the eigenfunctions have the same eigenvalues for the mirror operators, resulting in level repulsion.

5.2 Discussion

The model used in this thesis to find Dirac cones in two dimensional lattices is accurate for low energy ranges, yet it is also simplistic. The nearly free electron model is a valid approximation to the tight binding model in low energy ranges (see sections 2.3-2.5), but this does not take into account the complicated interactions of the electrons with the lattice, as it only considers nearest neighbour interactions. Other interaction terms are also neglected, such as the spin-orbit coupling of the electrons.

During our research we encountered several problems regarding the technological tools used for calculating the band structures. *Mathematica* is not optimally equipped for dealing with eigenvalue problems with complicated boundary conditions.

5.3 Outlook

There are several possibilities for future research in using the nearly free electron model as a tool for creating artificial lattices. One could, for example, look at triangular or other types of lattices. Another possibility is to take into account the interactions of the lattice beyond the nearest neighbour approximation, as well as the effects of the spin-orbit coupling of the electrons. In this thesis, we have assumed the electrons to be non-interacting and have neglected their spin orientation. Including this contributes to a more realistic description of electron behaviour in crystals, than the model described here.

6 Acknowledgement

I would like to thank my supervisors Prof. Dr. Cristiane de Morais Smith and Guido van Miert MSc at the Institute of Theoretical Physics at Utrecht University. Guido's door seemed always to be open whenever I had questions or doubts about this thesis. I never left his office without a renewed sense of motivation or ideas.

Author
Wies Uijttewaal

A The Effective Mass Theorem

Here we follow the method of Smith, Janak and Adler to explain the Effective Mass Theorem [8]. We start by replacing the Hamiltonian in the Schrödinger equation by an unperturbed Hamiltonian and a perturbation:

$$(H_0 + H')\psi_n(\vec{r}, t) = i\hbar \frac{\partial \psi_n(\vec{r}, t)}{\partial t} \tag{A.1}$$

The wave function $\psi_n(\vec{r}, t)$ is replaced by a wave packet centered around $k = 0$:

$$\psi_n(\vec{r}, t) = \int d^3 k A_{nk}(t) e^{i\vec{k} \cdot \vec{r}} u_{nk}(\vec{r}), \tag{A.2}$$

with A_{nk} an amplitude function, and $e^{i\vec{k} \cdot \vec{r}} u_{nk}(\vec{r})$ the Bloch functions, giving the result

$$\int d^3 k (E_n(\vec{k}) + H') A_{nk}(t) e^{i\vec{k} \cdot \vec{r}} u_{nk}(\vec{r}) = i\hbar \int d^3 k \dot{A}_{nk}(t) e^{i\vec{k} \cdot \vec{r}} u_{nk}(\vec{r}) \tag{A.3}$$

where we used the result of Bloch's Theorem: $H_0 e^{i\vec{k} \cdot \vec{r}} u_{nk}(\vec{r}) = E_n(\vec{k}) e^{i\vec{k} \cdot \vec{r}} u_{nk}(\vec{r})$. Bloch's Theorem also states that $E_n(\vec{k})$ is periodic in reciprocal space. This allows us to write

$$E_n(\vec{k}) = \sum_{\vec{R}_l} E_{nl} e^{i\vec{k} \cdot \vec{R}_l}, \tag{A.4}$$

with $\vec{R}_l$ the lattice vectors. Replacing $\vec{k}$ by $-i\vec{\nabla}$ requires that the following identity must hold:

$$E_n(-i\vec{\nabla}) = \sum_{\vec{R}_l} E_{nl} e^{\vec{R}_l \cdot \vec{\nabla}} \tag{A.5}$$

If we let this operator $E_n(-i\vec{\nabla})$ work on a function $f(\vec{r})$, we get:

$$E_n(-i\vec{\nabla}) f(\vec{r}) = \sum_{\vec{R}_l} E_{nl} e^{\vec{R}_l \cdot \vec{\nabla}} \vec{r}$$

$$\approx \sum_{\vec{R}_l} E_{nl} [1 + \vec{R}_l \cdot \vec{\nabla} + \frac{1}{2} (\vec{R}_l \cdot \vec{\nabla})(\vec{R}_l \cdot \vec{\nabla}) + \mathcal{O}(\vec{R}_l \cdot \vec{\nabla})] f(\vec{r})$$

$$= \sum_{\vec{R}_l} E_{nl} [f(\vec{r}) + \vec{R}_l \cdot \vec{\nabla} f(\vec{r}) + \frac{1}{2} \vec{R}_{l,\alpha} \vec{R}_{l,\beta} \frac{\partial^2}{\partial r_{,\alpha} \partial r_{,\beta}} f(\vec{r}) + \mathcal{O}(\vec{R}_l \cdot \vec{\nabla}) \quad = f(\vec{r} + \vec{R}_l) \tag{A.6}$$

We can also let it operate on a Bloch function, giving us:

$$E_n(-i\vec{\nabla}) \psi_{nk}(\vec{r}) = \sum_{\vec{R}_l} E_{nl} \psi_{nk}(\vec{r} + \vec{R}_l)$$

$$= \sum_{\vec{R}_l} E_{nl} e^{i\vec{k} \cdot (\vec{r} + \vec{R}_l)} u_{nk}(\vec{r} + \vec{R}_l)$$

$$= \sum_{\vec{R}_l} E_{nl} e^{i\vec{k} \cdot \vec{R}_l} e^{i\vec{k} \cdot \vec{r}} u_{nk}(\vec{r})$$

$$= \sum_{\vec{R}_l} E_{nl} e^{i\vec{k} \cdot \vec{R}_l} \psi_{nk}(\vec{r})$$

$$= E_n(\vec{k}) \psi_{nk}(\vec{r}). \tag{A.7}$$

Substituting this result into the Schrödinger equation gives us the Effective Mass Theorem:

$$[E_n(-i\vec{\nabla}) + H'] \psi_n(\vec{r}, t) = i\hbar \frac{\partial \psi_n(\vec{r}, t)}{\partial t}. \tag{A.8}$$

The original Hamiltonian has been replaced by an effective Hamiltonian in the form of the operator $E_n(-i\vec{\nabla})$, which is derived from the result of the perfect crystal. This operator can also be written as $\frac{p^2}{2m^*}$, in the case of a free particle ($V = 0$).

In order to apply the effective mass theorem, the dispersion relation of the perfect crystal, $E(\vec{k})$, must be known throughout the Brillouin Zone. If that is the case, perturbations on the crystal can be calculated in a relatively simple manner, without having to use the full Hamiltonian.
The Effective Mass Theorem can be applied in local regions in tight binding systems, where the dispersion relation can be specified or approximated on a part of the Brillouin Zone, for example with the NFE model. The EMT then provides a solution for the wave function in these regions.
If the dispersion relation is localised around $k = 0$, the Bloch functions can be expanded to:

$$\psi_n(\vec{r}) = e^{i(\vec{k}-\vec{k_0})\cdot\vec{r}}\psi_{nk_0}(\vec{r}).$$

This results in a new wave function

$$\psi_n(\vec{r},t) = \int d^3k A_{nk}(t) e^{i(\vec{k}-\vec{k_0})\cdot\vec{r}} u_{nk_0}(\vec{r}) \tag{A.9}$$

$$= F(\vec{r},t)\psi_{n_0}(\vec{r}), \tag{A.10}$$

where the function F represents an envelope function varying slowly in $\vec{r}$. This envelope function contains the information of the superlattice.

B Symmetry Operators

The symmetry of the lattice can be exploited to determine whether a band structure contains BCP's. There are several operations we can perform on the band structures obtained by (4.1). In this thesis we focus on two of these. In the first place, the mirror operator $\hat{M}$, operates on the eigenfunctions of the Hamiltonian. It gives us information regarding the symmetry of the energy bands along high symmetry lines. It determines whether an energy band in a particular region of the Brillouin Zone belongs to an even or an odd eigenfunction. This is useful, because we know that energy bands with equal symmetry do not form a band crossing point. Instead a band gap will appear when the disc/lattice ratio is increased. However, increasing this ratio will not result in a gap between two touching bands with opposite symmetry. This indicates the presence of a band crossing point. The operator works along the following equations:

$$\langle\psi|\hat{M}|\psi\rangle = \int dxdy\psi^*(x,y)\hat{M}\psi(x,y) = \pm 1, \tag{B.1}$$

where $\psi(x,y) = e^{\frac{i}{a_s}(k_x x + k_y y)}u_{k,n}(x,y)$ and $\hat{M}$ is the mirror operator along one of the high symmetry lines of the Brillouin Zone. On the region $\Gamma \rightarrow X$, the mirror operator $\hat{M}_y$ is used, with $\hat{M}_y\psi(x,y) = \psi(x,-y)$. On the region $X \rightarrow M$, $\hat{M}_x$ is used, with $\hat{M}_x\psi(x,y) = \psi(-x,y)$. On the region $M \rightarrow \Gamma$, $\hat{M}_{xy}$ is used, with $\hat{M}_{xy}\psi(x,y) = \psi(y,x)$.

A second operator that indicates BCP's is the rotation operator, $\hat{R}$. This is actually a special variant of the mirror operator, but instead of operating along high symmetry lines, it operates on high symmetry points. At these points (indicated by M in the Brillouin Zone) a double degeneracy is protected both by the four-fold rotation symmetry of the lattice as well as time-reversal symmetry. This is similar to the C_3 symmetry stabilising the Dirac points in the graphene lattice. The symmetries under C_4 rotation of the crossing energy bands are given by the eigenvalues of the rotation matrix:

$$\begin{pmatrix} \langle\psi_i|\hat{R}|\psi_i\rangle & \langle\psi_i|\hat{R}|\psi_j\rangle \\ \langle\psi_j|\hat{R}|\psi_i\rangle & \langle\psi_j|\hat{R}|\psi_j\rangle \end{pmatrix},$$

with

$$\langle\psi_i|\hat{R}|\psi_i\rangle = \int dxdy\,\psi_i^*(x,y)\hat{R}\psi_i(x,y) = \int dxdy\psi_i^*(x,y)\psi_i(-y,x). \tag{B.2}$$

References

[1] M. Polini, F. Guinea, M. Lewenstein, H. C. Manoharan, and V. Pellegrini, "Artificial honeycomb lattices for electrons, atoms and photons," *Nature Nanotechnology*, vol. 8, pp. 625–633.

[2] K. K. Gomes, W. Mar, W. Ko, F. Guinea, and H. C. Manoharan, "Designer Dirac Fermions and Topological Phases in Molecular Graphene," *Nature*, vol. 483, pp. 306–310, March 2012.

[3] A. Tadjine, G. Allan, and C. Delerue, "From lattice hamiltonians to tunable band structures by lithographic design," *Phys. Rev. B*, vol. 94, p. 075441, Aug 2016.

[4] E. Kalesaki, C. Delerue, C. Morais Smith, W. Beugeling, G. Allan, and D. Vanmaekelbergh, "Dirac Cones, Topological Edge States, and Nontrivial Flat Bands in Two-Dimensional Semiconductors with a Honeycomb Nanogeometry," *Phys. Rev. X*, vol. 4, p. 011010, Jan 2014.

[5] J. L. Mañes, F. Guinea, and M. A. H. Vozmediano, "Existence and topological stability of fermi points in multilayered graphene," *Phys. Rev. B*, vol. 75, p. 155424, Apr 2007.

[6] G. van Miert and C. M. Smith, "Dirac cones beyond the honeycomb lattice: A symmetry-based approach.," *Phys. Rev. B*, vol. 93, p. 035401, Jan 2016.

[7] B. A. Bernevig, *Topological Insulators and Topological Superconductors.* Princeton UP, 2013.

[8] A. C. Smith, J. F. Janak, and R. B. Adler, *Electron conduction in solids.* McGraw-Hill, New York, 1967.